Structure of *Helicobacter pylori* Catalase, with and without Formic Acid Bound, at 1.6 Å Resolution†

Peter C. Loewen,*,‡ Xavi Carpena,§ Carme Rovira,|| Anabella Ivancich,⊥ Rosa Perez-Luque,§ Rainer Haas,# Stefan Odenbreit,# Peter Nicholls,+ and Ignacio Fita§

Department of Microbiology, University of Manitoba, Winnipeg, MB R3T 2N2, Canada, Institut de Biologia Molecular de Barcelona, Consejo Superior de Investigacione Cientificas, Jordi-Girona 18-26, 08034 Barcelona, Spain, Centre de Recerca en Química Teòrica, Parc Científic de Barcelona, Josep Samitier 1-5, 08028 Barcelona, Spain, Service de Bioénergétique, URA 2096 CNRS, Département de Biologie Joliot-Curie, CEA Saclay, 91191 Gif-sur-Yvette, France, Max von Pettenkofer Institut, LMU München, München, Germany, and Department of Biological Sciences, University of Essex, Wivenhoe Park, Colchester CO4 3SQ, United Kingdom

Received September 15, 2003; Revised Manuscript Received December 15, 2003

ABSTRACT: *Helicobacter pylori* produces one monofunctional catalase, encoded by *katA* (hp0875). The crystal structure of *H. pylori* catalase (HPC) has been determined and refined at 1.6 Å with crystallographic agreement factors R and R_{free} of 17.4 and 21.9%, respectively. The crystal exhibits $P2_12_12$ space group symmetry and contains two protein subunits in the asymmetric unit. The core structure of the HPC subunit, including the disposition of a heme b prosthetic group, is closely related to those of other catalases, although it appears to be the only clade III catalase that has been characterized that does not bind NADPH. The heme iron in one subunit of the native enzyme appears to be covalently modified, possibly with a perhydroxy or dioxygen group in a compound III-like structure. Formic acid is known to bind in the active site of catalases, promoting the breakdown of reaction intermediates compound I and compound II. The structure of an HPC crystal soaked with sodium formate at pH 5.6 has also been determined to 1.6 Å (with R and R_{free} values of 18.1 and 20.7%, respectively), revealing at least 36 separate formate or formic acid residues in the HPC dimer. In turn, the number of water molecules refined into the models decreased from 1016 in the native enzyme to 938 in the formate-treated enzyme. Extra density, interpreted as azide, is found in a location of both structures that involves interaction with all four subunits in the tetramer. Electron paramagnetic resonance spectra confirm that azide does not bind as a ligand of the iron and that formate does bind in the heme pocket. The stability of the formate or formic acid molecule found inside the heme distal pocket has been investigated by calculations based on density functional theory.

The enzyme catalase protects organisms against reactive oxygen species through its degradation of hydrogen peroxide to water and oxygen (reaction 1) (*1*)

$$2H_2O_2 \rightarrow 2H_2O + O_2 \quad (1)$$

The reaction takes place in two two-electron reactions with the first hydrogen peroxide molecule oxidizing the heme to compound I, in which one oxidation equivalent is removed from the ferric iron, generating the oxoferryl species, and the other from the porphyrin ring to generate a porphyrin cation radical (reaction 2). The second hydrogen peroxide then reduces compound I to regenerate the resting (ferric) enzyme while releasing water and molecular oxygen (reaction 3).

$$\text{Enz (Por}-\text{Fe}^{III}) + H_2O_2 \rightarrow \text{Cpd I (Por}^{+\bullet}-\text{Fe}^{IV}{=}\text{O}) + H_2O \quad (2)$$

$$\text{Cpd I (Por}^{+\bullet}-\text{Fe}^{IV}{=}\text{O}) + H_2O_2 \rightarrow \text{Enz (Por}-\text{Fe}^{III}) + H_2O + O_2 \quad (3)$$

At limiting H_2O_2 concentrations, catalases may suffer a one-electron reduction to an inactive intermediate, compound II (reaction 4), which can subsequently be converted to another inactive form, compound III (reaction 5).

$$\text{Cpd I (Por}^{+\bullet}-\text{Fe}^{IV}{=}\text{O}) + HA \rightarrow \text{Cpd II (Por}-\text{Fe}^{IV}-\text{OH}) + A^{\bullet} \quad (4)$$

† This work was supported by Grants BQU2001-04587-CO02 and BIO2002-04419 from Ministerio de Ciencia y Technologia (MCYT) to C.R. and I.F., respectively, by Grant 2001SGR-00044 from the Comissió Interdepartamental de Recerca i Innovaciò Tecnològica (CIRIT) to C.R., and by Grant OGP9600 from the Natural Sciences and Engineering Research Council of Canada (NSERC) to P.C.L. Computer resources were provided in part by the CEPBA-IBM (Centre Europeo de Paralálelisme de Barcelona) Research Institute of Barcelona.

* To whom correspondence should be addressed: Department of Microbiology, University of Manitoba, Winnipeg, MB R3T 2N2, Canada. Phone: (204) 474-8334. Fax: (204) 474-7603. E-mail: peter_loewen@umanitoba.ca.

‡ University of Manitoba.

§ Consejo Superior de Investigacione Cientifícas.

|| Centre de Recerca en Química Teòrica.

⊥ URA 2096 CNRS.

LMU München.

+ University of Essex.

10.1021/bi035663i CCC: $27.50
Published on Web 02/27/2004

$$\text{Cpd II (Por}-\text{Fe}^{IV}-\text{OH}) + H_2O_2 \rightarrow \text{Cpd III (Por}-\text{Fe}^{II}=\text{OOH}^{+}) + H_2O \quad (5)$$

The catalase reaction has evolved in at least three phylogenetically unrelated protein types, including the monofunctional or "classical" catalase, the bifunctional catalase peroxidase, and the non-heme or Mn-containing catalase (*1*). The most extensively characterized class is the monofunctional catalases which were first reported in 1900, and have subsequently been found in both small subunit (55−60 kDa) and large subunit (78−84 kDa) forms. The crystal structures of eight such monofunctional catalases have been determined, including the enzymes from bovine liver (*2*, *3*), *Penicillium vitale* (*4*, *5*), *Micrococcus lysodeikticus* (*6*), *Proteus mirabilis* (*7*), *Escherichia coli* (*8*, *9*), *Saccharomyces cerevisiae* (*10*, *11*), human erythrocytes (*12*, *13*), and *Pseudomonas syringae* (*14*, *15*).

The catalytic properties of the catalase of *Helicobacter pylori* (HPC)[1] are very similar to those of other catalases, although it is somewhat more resistant to inhibition by cyanide and aminotriazole (*16*). Despite these average properties, the enzyme is particularly effective in protecting the bacteria against oxidative bursts by polymorphonuclear granulocytes, and this may, at least in part, be a result of some of the enzyme being located externally, possibly on the cell surface (*17*). The structural analysis of HPC reported here was, in part, undertaken to determine if there were any features that might be consistent with an external location or that explain its effectiveness.

Formic acid reacts with catalases in at least three ways: to become a ligand with the heme iron, to serve as an electron donor for compound I reduction, and to stimulate compound II decay (*1*, *18*). The structures of catalases with several common inhibitors, including cyanide, azide, and aminotriazole, and of an acetate complex have been reported, but to date, no structure of formic acid bound to a heme-containing protein has been reported. This paper also describes the locations of binding of formic acid to HPC. A theoretical analysis of the stability of the formate or formic acid molecule found in the distal side heme pocket, together with EPR evidence for its presence, is presented.

MATERIALS AND METHODS

Crystallization and Data Treatment. The catalase gene, *katA* or hp0875, was cloned from *H. pylori* strain P1 in plasmid pSO100 (*17*). The HPC protein analyzed in this work was purified from the catalase deficient *E. coli* UM255 as previously described (*16*). Crystals were obtained at room temperature by the vapor diffusion hanging drop method at a protein concentration of ∼6 mg/mL over a reservoir containing 15% PEG MME 550, 0.1 M sodium citrate (pH 5.6), 10 mM $ZnSO_4$, and 3 mM NaN_3. The crystallization buffer was supplemented with 10 mM sodium formate for a 5 s soaking and 20 mM sodium formate for a 1 s soaking. Crystals were orthorhombic, in space group $P2_12_12$, with two subunits in the crystal asymmetric unit. Diffraction data were obtained from crystals cooled with a nitrogen cryostream, giving the following unit cell parameters: $a = 64.3$ Å, $b = 154.5$ Å, $c = 95.8$ Å, and α, β, and $\gamma = 90.0°$. The diffraction data set was processed using MOSFLM (*19*) and scaled with SCALA (*20*). Five percent of the measured reflections in every data set was reserved for R_{free} monitoring during automatic refinement (Table 1).

Structure determination was carried out with MOLREP (*21*) using PMC with the appropriate residue changes to reflect the HPC sequence as the initial searching model. Refinements were completed using REFMAC (*22*) with solvent molecules modeled with WATPEAK (*19*) and manually with O (*23*). Solvent molecules were only introduced when they corresponded to the strongest peaks in the difference Fourier maps that could make at least one hydrogen bond with atoms already in the model. In the final rounds of refinement, the two subunits were treated independently with the bulk solvent correction applied and the whole resolution range available used for each variant. The analysis of solvent accessibility and molecular cavities was carried out with VOIDOO (*24*) using a reduced atomic radius for polar atoms in accounting for possible hydrogen bonds (*25*). All figures were prepared using SETOR (*26*).

Structure factors and coordinates have been submitted to the Protein Data Bank as entries 1QWL (native) and 1QWM (with formate).

Affinity Chromatography. Catalases, including HPC, HPII, and yeast CATA, were applied to Affi-Gel Blue affinity gel (Bio-Rad), and bound enzyme was eluted with NADPH as described previously (*27*).

EPR Spectroscopy. Conventional 9 GHz EPR measurements were performed using a Bruker ER 300 spectrometer with a standard TE102 cavity equipped with a liquid helium cryostat (Oxford Instrument) and a microwave frequency counter (Hewlett-Packard 5350B). Catalase samples (0.2 mM) in 0.05 mM Tris-maleate buffer (pH 7.4) were measured in standard 4 mm diameter quartz tubes. Native catalase samples were treated with a 50- and 100-fold excess of azide and sodium formate (pH 7.4), respectively. Experimental conditions were as follows: temperature, 4.2 K; microwave frequency, 9.42 GHz; modulation amplitude, 4 G; modulation frequency, 100 kHz; microwave power, 1 mW; and two scans.

Theoretical Calculations. Theoretical calculations using density functional theory (DFT) were carried out to investigate the formate or formic acid molecule bound in the distal heme cavity. Because the positions of the hydrogen atoms are not available from the X-ray analysis, and it is not clear whether the ligand is present as formate anion or formic acid, several possibilities were considered using either large (up to 87 atoms) or small (up to 43 atoms) models. On the distal side, both His56 and Asn129 residues might directly hydrogen bond to the formate or formic acid ligand. On the proximal side, Arg335 is hydrogen bonded to Tyr339, the heme iron proximal ligand, and influences the binding of a distal ligand to the heme iron (*28*). Therefore, the large models included the formate or formic acid ligand, Arg335 (replaced with a methylguanidinium cation), Tyr339 (replaced with a phenolate anion), His56 (replaced with a methylimidazole molecule), Asn129 (replaced with an ac-

[1] Abbreviations: HPII, catalase from *E. coli*; BLC, bovine liver catalase; CATA, *S. cerevisiae* catalase; PMC, *P. mirabilis* catalase; HEC, human erythrocyte catalase; MLC, *Micrococcus luteus* catalase; HPC, *H. pylori* catalase; PVC, *Pe. vitale* catalase; EPR, electron paramagnetic resonance.

Table 1: Data Collection and Structural Refinement Statistics for HPC with and without Formic Acid Bound

	native	with formate
data collection		
space group	$P2_12_12$	$P2_12_12$
a (Å)	64.26	64.76
b (Å)	154.50	154.96
c (Å)	95.76	96.16
α, β, γ (deg)	90	90
resolution range (Å)	29.5−1.6 (1.69−1.6)[a]	29.9−1.6 (1.69−1.6)
no. of unique reflections ($F > 0$)	119259 (7699)	124796 (8557)
completeness (%)	94.4 (87.3)	97.4 (92.5)
$\langle I/\sigma(I)\rangle$	13.6	16.0
R_{sym} (%)[b]	6.0 (13.7)	4.7 (17.9)
refinement		
working set	113241 (7337)	118512 (8128)
no. of free reflections	6018 (362)	6284 (429)
R_{cryst} (%)[c]	17.4 (22.0)	18.1 (20.0)
R_{free} (%)	21.9 (28.0)	20.7 (23.0)
no. of non-hydrogen atoms		
proteins	8127	8081
waters	1016	938
hemes	86	86
oxygens	2	−
formic acids	−	108
rmsd from ideality		
bond lengths (Å)	0.02	0.02
bond angles (deg)	1.8	1.6
planarity (Å)	0.01	0.01
estimated coordinate error (Luzzati) (Å)	0.18	0.16
averaged B factor (Å^2)		
main chain	10.84 (A, 11.72; B, 9.95)	12.78 (A, 13.71; B, 11.84)
side chain	12.43 (A, 13.00; B, 11.85)	15.10 (A, 16.00; B, 14.20)
water	19.52	23.00
oxygen	21.78	
formate	−	37.94

[a] Values in parentheses correspond to the highest-resolution shell. [b] $R_{sym} = \sum_{hkl}\sum_j |I_{hkl,j} - \langle I_{hkl}\rangle|/\sum_{hkl}\langle I_{hkl}\rangle$. [c] $R_{cryst} = \sum||F_o| - |F_c||/\sum|F_o|$. R_{free} is as for R_{cryst} but calculated for a test set comprising reflections not used in the refinement.

etamide molecule), and the heme moiety (replaced with an iron porphyrin).

Calculations were performed with the ligand present either as formic acid, interacting with N_δ of Asn129 either through the hydroxyl or through the carbonyl oxygen, or as a formate anion, keeping the His56 residue neutral in all cases. The total spin of the system (S) was always taken to be $^5/_2$ [high spin, the experimental ground state for the five-coordinated heme in catalases as observed in the EPR spectrum (see the Results)].

When large model calculations suggested that interaction of the heme with the formate or formic acid ligand was negligible, small models were used for molecular dynamics simulations. These small models included just the ligand and distal residues His56 (replaced with a methylimidazole molecule) and Asn129 (replaced with an acetamide molecule), in addition to Ser95 (replaced with methanol) and Thr96 (replaced with formaldehyde), which hydrogen bond to His56, and a water molecule which is hydrogen bonded to the OH group of Ser95.

Computations were performed using the CPMD 3.0h program written by J. Hutter (1998, Max-Planck-Institut für Festkörperforschung, Stuttgart, Germany) which uses the Car−Parrinello molecular dynamics method based on DFT (*29*, *30*). Previous work has demonstrated the reliability of this method in the description of structural, energetic, and dynamical properties of molecules of biological interest, including heme proteins (*31*, *32*). The Kohn−Sham orbitals are expanded in a plane wave basis set with a kinetic energy cutoff of 70 Ry. We employed *ab initio* pseudopotentials, generated within the Troullier−Martins scheme (*33*), including the nonlinear core correction (*34*) for the iron atom. Our calculations were carried out using the generalized gradient-corrected approximation of the spin-dependent density functional theory (DFT-LSD), following the prescription of Becke and Perdew (*35*, *36*). Molecular dynamics simulations were performed using a time step of 0.12 fs, and the fictitious mass of the electrons was set at 900 au. The energy minimizations were carried out by means of molecular dynamics with annealing of the atomic velocities. The systems are enclosed in an isolated supercell: 11 Å × 15 Å × 17 Å for large models and 12 Å × 15 Å × 12 Å for small models. The size of the model used (up to 87 atoms) is at the limit of what can be done using first-principles methods. The iron porphyrin and the residue models, whose movement is restrained by the protein, were considered partially fixed, and only the position of their hydrogen atoms was optimized. This allows a reproduction of the elongation of the X−H distances (X being O or N) when possible hydrogen bonds are formed and a proper description of the energy and structural properties of these bonds (*28*).

RESULTS

Quality of the HPC Model. The electron density map defines main chain and side chain atoms of 982 amino acids and two heme groups in two subunits, named A and B, and

```
MVNKDVKQTTAFGAPVWDDNNVITAGPRGPVLLQSTWFLEKLAAFDRERIPERVVHAKGS      60
                                                          56
GAYGTFTVTKDITKYTKAKIFSKVGKKTECFFRFSTVAGERGSADAVRDPRGFAMKYYTE     120
                                    97              109
EGNWDLVGNNTPVFFIRDAIKFPDFIHTQKRDPQTNLPNHDMVWDFWSNVPESLYQVTWV     180
        129                                               175 179
MSDRGIPKSFRHMDGFGSHTFSLINAKGERFWVKFHFHTMQGVKHLTNEEAAEIRKHDPD     240
    184
SNQRDLFDAIARGDYPKWKLSIQVMPEEDAKKYRFHPFDVTKIWYTQDYPLMEVGIVELN     300
                                          283 286
KNPENYFAEVEQAAFTPANVVPGIGYSPDRMLQGRLFSYGDTHRYRLGVNYPQIPVNKPR     360

CPFHSSSRDGYMQNGYYGSLQNYTPSSLPGYKEDKSARDPKFNLAHIEKEFEVWNWDYRA     420

DDSDYYTQPGDYYRSLPADEKERLHDTIGESLAHVTHKEIVDKQLEHFKKADPKYAEGVK     480

KALEKHQKMMKdmhgkdmhhtkkkk                                         505
```

FIGURE 1: Sequence of HPC. The 14 C-terminal residues that are missing in the structure are lowercase letters. Specific residues that are mentioned in the text are indicated with a residue number below.

1016 water molecules. The maps show clear continuity in both subunits over the complete length from Met1 to Lys491. Fourteen residues at the C-terminus predicted from the gene sequence (Figure 1) are not evident in the maps and are presumed to be disordered. The model has crystallographic agreement R and R_{free} values of 17.4 and 21.9%, respectively, for 126 958 reflections in the resolution shell between 1.6 and 29.5 Å. The average root-mean-square deviation (rmsd) after superimposition of the two subunits is 0.24 Å for the Cα atoms and 0.48 Å for all atoms. The average temperature factor values for the main and side chain atoms of the two subunits are very similar, 11.7 and 13.0 Å^2 for subunit A as compared to 10.0 and 11.9 Å^2 for subunit B, respectively.

Ramachandran plots confirm that only one residue, Ser198, lies outside the energetically favorable regions in both subunits. This residue is equivalent to the residues in other catalases (Val219 in CatF, Ser216 in BLC, Ser196 in PMC, Ser217 in PMC, and Ser and Ile274 in HPII) that are also found in an energetically unfavorable conformation. In CATA, the equivalent residue is a Gly. These residues are located adjacent to the heme at the beginning of the lateral channel, but a role for the unusual conformation at the location has not been determined.

Overall Structure. The molecular form of the HPC enzyme, like all other catalases, is a tetramer with an accurate 222 point group symmetry, also defined by the molecular P, Q, and R axes (Figure 2). The tetramer has dimensions very similar to those of other small subunit catalases along the P, Q, and R molecular axes (∼100 Å × ∼60 Å × ∼100 Å, respectively). In the HPC structure, the molecular R axis is coincident with a 2-fold crystallographic axis, which leaves only the dimer of subunits A and B in the asymmetric unit, and these are crystallographically related to subunits D and C, respectively. The structural differences between subunits A and B are, therefore, also present between subunits C and D, leading to the R-related A−D and B−C dimers differing similarly to what has been reported for CatF and HEC (taking into account a nomenclature correction of subunits C and D).

The general folding of the HPC model is very similar to the folding of the six other small subunit catalases and of the 550 amino-terminal residues of the two large subunit catalases. After superimposition, the average rmsd values for 368 core Cα atoms (with any intervening regions in longer sequences removed to eliminate gaps) were 1.02 with CatF, 1.07 with HPII, 1.18 with PVC, 0.89 with MLC, 0.81 with PMC, 1.46 with CATA, 1.24 with BLC, and 1.25 with HEC. The four regions typical of small subunit catalases, including the N-terminal arm (to Val55), an antiparallel eight-stranded β-barrel (residues His56−Ala314), an extended wrapping loop (Phe315−Gln428), and a helical domain at the carboxy terminus (Pro429−Met491), are evident in the HPC monomer structure (Figure 3). The heme is oriented with the imidazole ring of the essential His above ring III (His-III), which is the orientation common to all other clade 3 catalases, but different from the His-IV orientation found in clade 1 and 2 catalases.

The intertwining or "arm exchange" of subunits, another feature unique to catalases that makes subunit folding and subunit association deeply interconnected processes, occurs with symmetrically related subunits in the tetramer. In HPC, a relatively short length of seven N-terminal residues protrudes through the loop with subunit A interacting with subunit C and subunit B with subunit D. The presence of two alternate conformations for the main chain atoms of Arg101 and Gly102, differing by a 180° flip about the peptide bond, is another structural oddity previously noted in HEC, CatF, PVC, and MLC, but not the other catalases. The subunit pairs, A and D and B and C, associate in one of two complementary conformations, both of which break the 2-fold crystallographic symmetry. The symmetric conformation with both carbonyl oxygens pointing toward the opposing subunit is unlikely because of steric conflicts. Despite it being close to the heme active site center, there is still no evidence supporting the conjecture that the break in symmetry may have a functional role, and its presence in only some catalases presents further difficulties in interpretation.

NADPH and Azide Binding. Of the catalases for which structures are available, NADPH binds to all of the clade 3 enzymes, either very tightly as in BLC, HEC, and PMC or with lower affinity as in MLC or CATA, and the binding site structures are highly conserved. On the other hand,

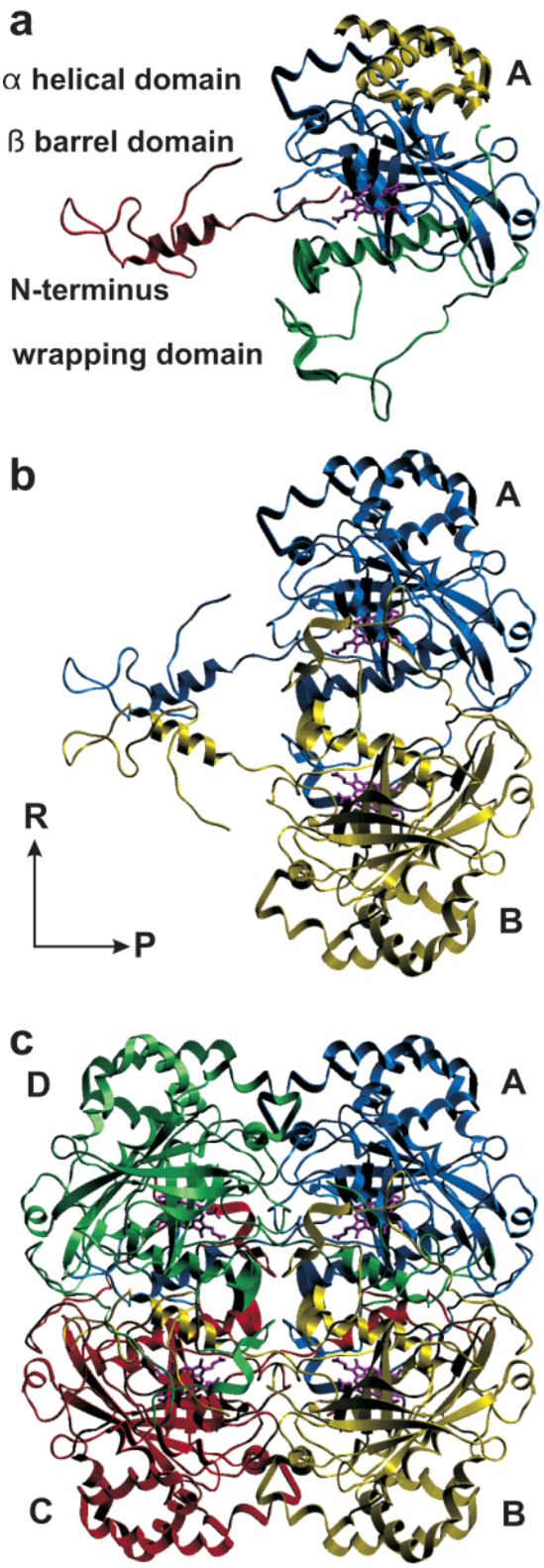

FIGURE 2: Views of HPC to illustrate the relationship of the subunits. (a) Subunit A with the N-terminal domain colored red, the *β*-barrel domain colored blue, the α-helical domain colored yellow, and the wrapping domain colored green. (b) Dimer composed of subunits A and B that make up the asymmetric unit in the crystal. Subunit A is colored blue and subunit B yellow. (c) Tetrameric structure of HPC prepared from subunits A (blue) and B (yellow), and their symmetry-related equivalents, subunits D (green) and C (red). The orientation of the *R* and *P* axes is shown. The *Q* axis is perpendicular to the figure.

NADPH does not bind to the clade 1 catalase, CatF, or to the large subunit clade 2 enzymes, HPII and PVC, where the putative binding sites deviate significantly from those in clade 3 enzymes. It was therefore expected that HPC, a clade 3 enzyme, would bind NADPH, but no electron density consistent with its presence is evident in the maps. Indeed, the final $F_o - F_c$ difference Fourier map contains no significant positive density throughout the model, including the region of expected NADPH binding, and the $2F_o - F_c$ difference Fourier map is consistent with a small number of clearly defined waters in the expected NADPH binding site (Figure 3). $F_o - F_c$ maps calculated with the water molecules omitted from the model in the vicinity of the putative NADPH binding site contained only density that can be attributed to the missing waters. HPC did not bind to Affi-Gel Blue, an affinity column for NADPH-binding proteins, whereas yeast CATA did bind (data not shown), confirming that HPC either does not bind NADPH or does so very weakly.

A small region of electron density in the final $F_o - F_c$ difference Fourier map is present on the *P* axis near what would be the central cavity of the tetramer (Figure 4). This is well removed from the surface location of NADPH binding, and ~15 Å from the expected location for azide binding near the heme iron. However, refinement with azide in the model resulted in the disappearance of all residual density in the $F_o - F_c$ difference Fourier map. In this location, the azide is associated with one arginine residue (Arg47) from each subunit in the symmetrically related dimer (subunits C and D of the tetramer) and makes van der Waals contact with the main chain atoms of Tyr345 from both subunits A and B and with the phenyl ring of Tyr345 in subunit A.

Channel Structure. HPC presents a channel structure that differs from those of other small subunit catalases. The lower part of the channel up to the conserved Asp109 is narrower by 0.5−1 Å than those of other enzymes, a result of small shifts in the locations of Phe134 and Phe145 and the presence of Ile146 in place of a Val in many other catalases. In comparison with the wide channel in CatF, the narrow channel in HPC presents a significant gap in the surface map adjacent to the conserved Val (Figure 5a). Just beyond the conserved Asp109, the channel abruptly opens into a chamber or cavity, a significant deviation from the funnel shape observed in PMC, HEC, BLC, and CatF (Figure 5b). Only CATA exhibits a similar cavity structure (Figure 5c), but the opening to the exterior is larger than in HPC. The channel structure of HPC might be considered as a hybrid of the CATA channel and the channel of MLC in which there is a very distinct small cavity with narrow exits (Figure 5d).

In the narrow part of the channel below Asp109, there are only four water molecules evident in equivalent locations in both subunits (Figure 6). For comparison with other catalases, the water numbering system employed for CatF (*15*) is used, and waters I, II, and III, conserved in all catalase structures, are included for reference. The single water in the distal heme cavity at position 2 is conserved in most catalase structures and interacts with both the imidazole of His56 and the side chain of Asn129. There are no waters in the hydrophobic region around the conserved Val where waters are found in some catalases (position 3), and the next two waters are located at positions 4 and 4b close to the

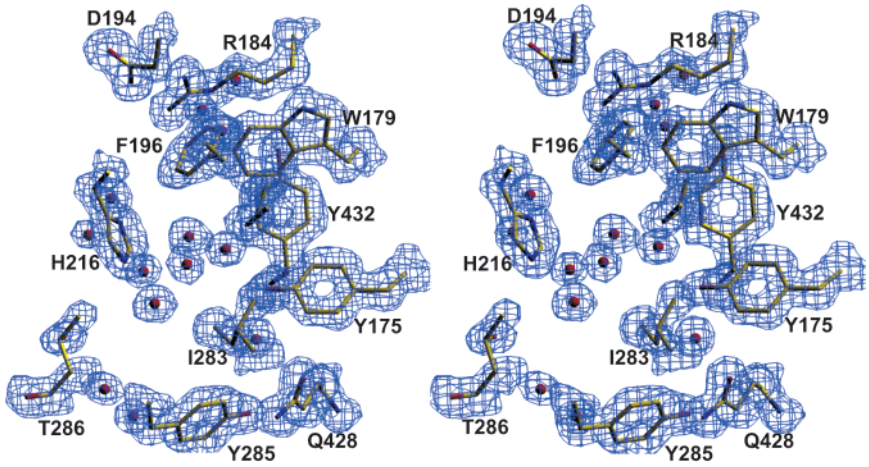

FIGURE 3: Stereoview $2F_o - F_c$ (blue) and $F_o - F_c$ (red) electron density map of the potential NADPH-binding site on HPC. The $2F_o - F_c$ density is modeled at 1.0σ and the $F_o - F_c$ density at 3.0σ. Waters are depicted as red spheres.

conserved Asp129. The water at position 5b has an equivalent in HPII. The waters at positions 6 and 7 lay at the transition between the narrow channel and larger cavity, where the pattern of waters diverges considerably from that in other catalases.

Heme Iron Ligand. The distal heme pockets of the two subunits present quite different patterns of electron density. No waters are evident in position 1 (CatF and HPII numbering), the sixth ligand position above the heme iron in either subunit. However, subunit A exhibits a region of strong electron density in the proximity of the heme iron in omit maps (Figure 6a) that is absent in the maps of subunit B (Figure 6d). This is the expected location for azide binding in catalase, but azide in the model did not provide a satisfactory solution, presenting density in the $F_o - F_c$ Fourier maps and distorting the density in the $2F_o - F_c$ maps (Figure 6c). Refinement with a dioxygen group covalently attached to the Fe in the HPC model, reminiscent of a compound III structure, produces an excellent fit to the density. O2 is placed 1.83 Å from the heme iron and O1 2.09 Å from the water at position 2, and all density is eliminated from the $F_o - F_c$ maps (Figure 6b).

The low-temperature (4 K) 9 GHz EPR signal of native HPC showed the typical pattern of a pentacoordinated high-spin ($S = {}^5/_2$) ferric heme iron with two main resonances at $g^{eff}{}_{\perp} \approx 6$ and $g^{eff}{}_{||} \approx 2$ (Figure 7a). The effective g values ($g_x = 6.36$, $g_y = 5.35$, and $g_z = 1.98$) were very similar to those previously observed for bovine liver and *P. mirabilis* catalases (*37*) and agree well with the structural similarities observed in the crystal structures of these enzymes as compared to subunit B in HPC. An additional EPR signal, with effective g values ($g_1 = 2.43$, $g_2 = 2.06$, and $g_3 = 1.87$) characteristic of a weak field ligand to the sixth position of the ferric heme iron, was also detected (Figure 7 inset); spin quantification indicated a maximum of a 20% contribution of this other signal, although this percentage appeared to be preparation-dependent. EPR signals with similar g values were previously reported for peroxidases (*38*, *39*) and were attributed to a water (or hydroxy) molecule acting as a sixth ligand to the heme. It is noteworthy that EPR signals with g values of 2.31, 2.18, and 1.94 (g_1, g_2, and g_3, respectively) were assigned to a hydroperoxyferriheme species in myoglobin (*40*, *41*). Accordingly, the presence of the low-spin signal in the EPR spectrum of HPC is consistent with the proposal of a dioxygen species attached to the heme iron in subunit A.

Coordination of an azide molecule to the heme iron should induce a change in the spin state of the ferric iron from high to low spin, causing a dramatic change in the EPR spectrum. Specifically, all the high-spin ferric signal of the native catalase with a $g^{eff}{}_{\perp}$ of ≈6 and a $g^{eff}{}_{||}$ of ≈2 (Figure 7a) should be replaced by a low-spin signal with a $g^{eff}{}_{||}$ of ≈2. Such changes are not observed in the EPR spectrum of the azide-treated sample (Figure 7c), leading to the conclusion that azide is not bound in the sixth coordination position, consistent with the absence of an axial ligand azide in the heme cavity in the crystal structure (Figure 6). The spectral changes that are observed for the azide-treated enzyme are consistent with changes in the heme environment, similar to those induced by pH modifications [compare spectra A (at pH 5.4) and C in the center inset of Figure 7].

Formate and Formic Acid Binding. Formic acid binds to catalases, can donate an electron to compound I, and promotes the degradation of compound II. Its mode of interaction with catalases was therefore of interest, and the possible presence of an oxoferryl species in subunit A made HPC an especially appealing target. The structure of a crystal soaked in sodium formate (pH 5.6) was therefore refined to 1.6 Å (Table 1), revealing 36 formic acid molecules in the dimer. The locations of the formic acids were all checked in omit maps generated with models lacking formic acid and by density averaging of the two subunits. Typically, the electron density manifested itself as an elongated and slightly bent shape, and where there was any doubt, formic acid was not included.

Five groups of formic acids can be discerned (Table 2) on the basis of their locations in the dimer. The first and mechanistically most interesting location is in the distal heme cavity and main channel. One formic acid is found adjacent to the heme in both subunits, although not exactly in the same locations in the two subunits, being 2.66 and 3.88 Å from the heme iron in subunits A and B, respectively (Figure 8). To create room for the formic acid molecules, the putative dioxygen group linked to the heme iron in subunit A and waters at position 2 of both subunits of the native structure have been displaced. The asymmetry in the formic acid location between the two subunits is also further evident up the main channel (Figure 8) where there are two molecules

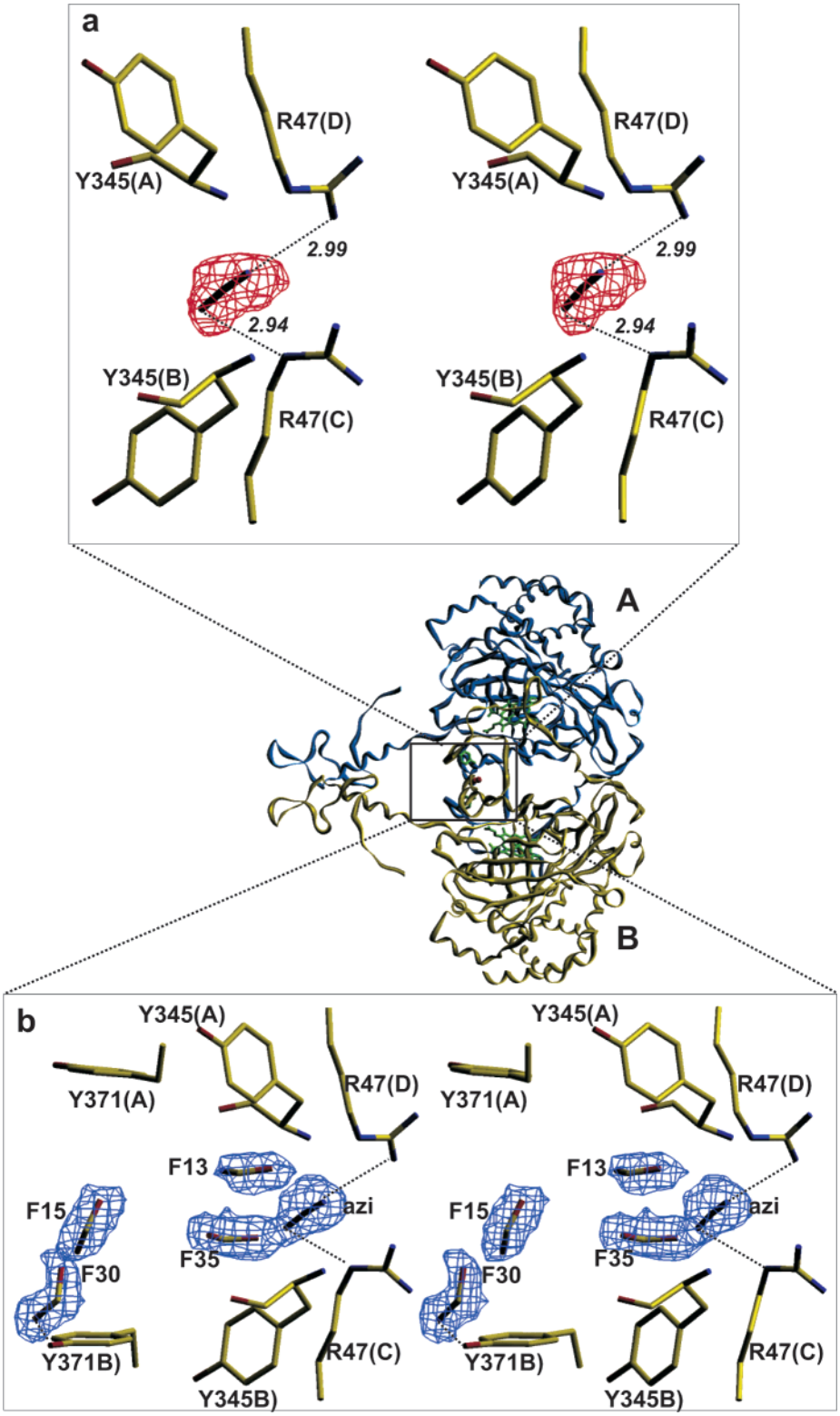

FIGURE 4: Stereoview of the region along the *P* axis of the dimer that includes the putative azide binding site. The region of the dimer that is expanded in panels a and b is outlined by the box. (a) View of the omit $F_o - F_c$ electron density (red) of the region generated without azide included in the model during refinement. Introduction of azide into the model resulted in its positioning as shown and a loss of the density in the $F_o - F_c$ map (not shown). The density is modeled at 3.0σ. (b) View of the $2F_o - F_c$ electron density (blue) corresponding to azide and formic acid molecules. The electron density is modeled at 1.0σ. The formate numbering corresponds to that in Table 2.

in subunit A and four in subunit B, of which only two (F6 in subunit A and F7 in subunit B) are symmetrically related. These six formic acids are all situated in the expanded or cavity portion of the channel above the conserved Asp109.

Eight formic acids or formate anions are found at the interface between the two subunits in and around the central cavity (Figure 4b). Six are at the interface between two dimers forming the tetramer. Eleven are in a relatively small area on the surface of the subunits. Three are scattered with no apparent pattern. Finding this many formic acids in the structure was a surprise, and it is not possible to explain why they bind where they do in every case. Waters are not

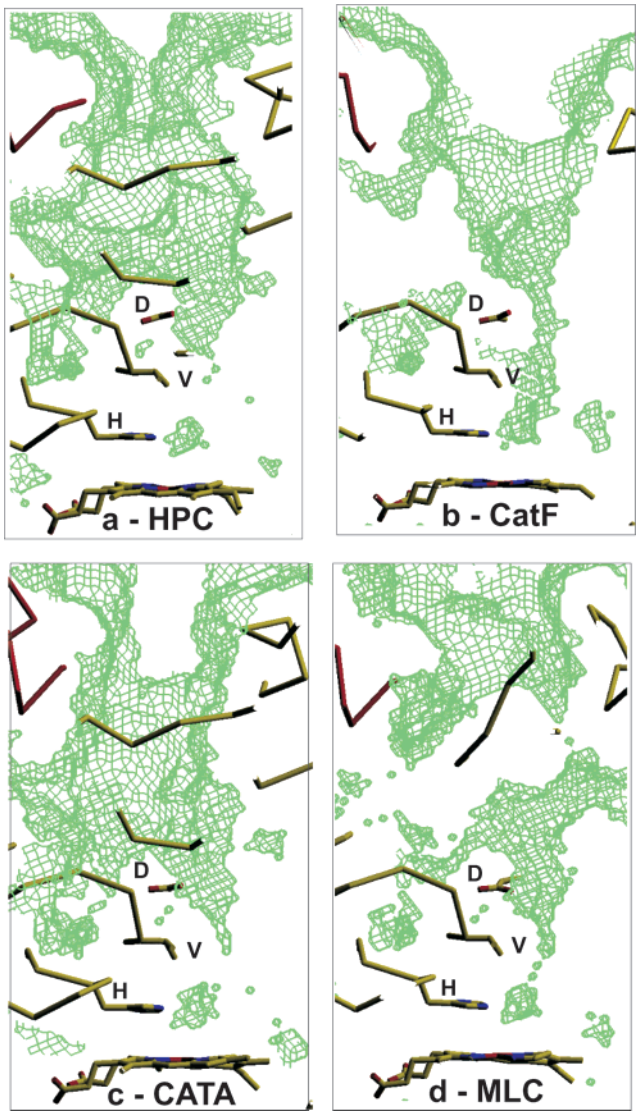

FIGURE 5: View of the channels leading to the active sites in various catalases. The accessibility surfaces, determined using VOIDOO, are shown as green lattices and are a reflection of what parts of the protein are accessible to a molecule approximately the size of water. The cross section or slab is chosen to illustrate most clearly the features of the channel, and the orientation is approximately the same in each enzyme. The three residues conserved in all catalases are (using HPC numbering) H (His56), V (Val97), and D (Asp109): (a) HPC, (b) CatF, (c) CATA, and (d) MLC.

displaced at nine formic acid binding sites, and 11 formic acids make contact with only water or other formic acid molecules, not with the protein. Eleven formic acids in each subunit have a symmetry-related partner in the second subunit (around the *P* axis), but this leaves 14 molecules that break the symmetry between the two subunits.

Modifications in the coordination environment of the heme iron in catalases and peroxidases can be monitored by the extent of rhombic distortion on the EPR signal, reflected by differences between the g_x and g_y components of the **g** tensor. The difference in **g** anisotropy (or rhombic distortion) of the two signals can be directly correlated to geometry changes in the heme environment (*42*). For example, pH changes are known to induce modifications in the EPR spectrum of catalases (*43*) similar to those in the spectra of HPC (Figure 7 inset). The EPR spectrum of HPC treated with formate (Figure 7b) reveals another ferric (high-spin) signal, with *g* values ($g_x = 6.62$, $g_y = 5.35$, and $g_z = 1.96$) different from those of the native enzyme ($g_x = 6.36$, $g_y = 5.35$, and $g_z = 1.98$), and is similar to the spectrum of the native enzyme at low pH (Figure 7, center inset). Significantly, the low-spin ferric signal, consistent with the dioxygen species, was absent in the spectrum of the formate-treated enzyme. This is consistent with the presence of formic acid in two locations (presumably one in each subunit) in the distal heme cavity and removal of the putative perhydroxy group from the heme iron (Figure 8) as suggested by the electron density maps.

Theoretical Calculations. Four possible situations, two for the formic acid molecule, one for the formate anion and a protonated imidazole, and one for formate anion alone bound in the heme pocket, and their optimized structures are shown in Figure 9. The two structures with formic acid converge to minima where the ligand is hydrogen bonded with His56 and Asn129 in configurations similar to the model in subunit B (Figure 9a,b). Apart from the position of the carboxylic proton and a small difference in rotation, the two minima with formic acid have similar structures and energies, situation 9a being 1.6 kcal/mol less stable than situation 9b. The formic acids are situated 3.7 Å (in Figure 9a) and 4.4 Å (in Figure 9b) from the heme iron, indicative of very little interaction between the formic acid ligand and the heme. Indeed, removing the heme and the proximal residues from the calculations produced the same results with respect to the position of the ligand and the relative energy of the conformations.

Simulations with formate anion (Figure 9c) result in the repulsive interaction between formate O^- and Nϵ of His56, forcing the ligand away from the imidazole ring, leaving it hydrogen bonded with only the NH_2 group of Asn129. In addition, the molecular plane of the formate is almost perpendicular to the NH_2 plane, and the ligand placement is inconsistent with the actual ligand locations in either subunit A or B. Starting the calculations with the formate ligand positioned as in subunit A or subunit B did not change the results.

To investigate the stability of a structure with the carboxylic proton transferred to the imidazole ring of His56, a dynamic analysis in a small system was performed. Both Ser95 and Thr96, which hydrogen bond to the N_δ hydrogen of the imidazole (from −OH and C═O, respectively), were included in the model, and variations in temperature of the system were considered in molecular dynamics simulations. Transfer of the proton back and forth between the carboxyl proton (His···HCOOH) and the imidazole ring (His-H^+···$^-$-OOCH) occurs three to five times per picosecond, with a corresponding oscillation of the COO plane with respect to the imidazole plane of 60° (Figure 10). The interchange of the COOH proton involves the same carboxylate oxygen within the time scale (5 ps) that was followed, and a longer simulation time would be required to exclude the possibility of proton exchange between carboxylate oxygens via Nϵ of imidazole.

In the case of the conformation in Figure 9a, one of the formic acid oxygens is not involved in any hydrogen bonds and, therefore, would be free to interact with the heme iron if formic acid transfers its proton to His56. To test this hypothesis, additional calculations were performed in a large model with residues Ser95 and Thr96 added to the model in

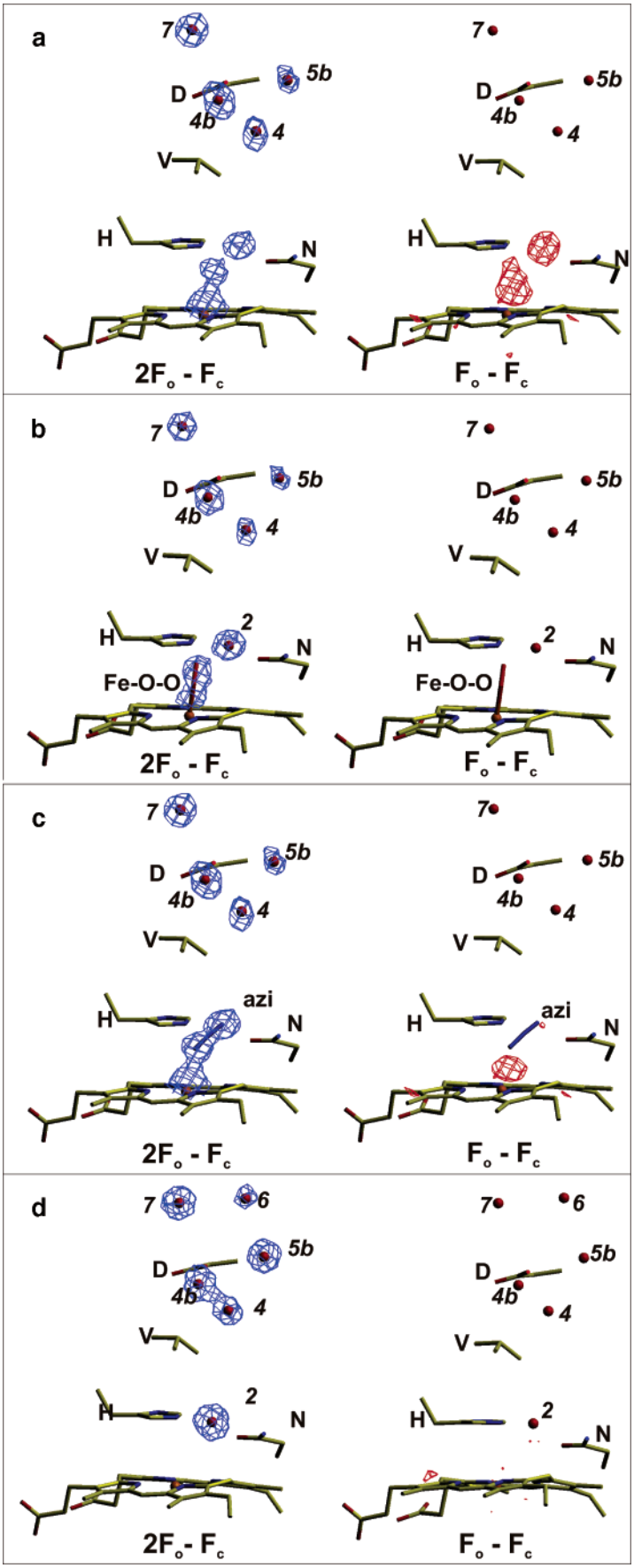

FIGURE 6: Views of the distal heme cavities and main channels of the two subunits of HPC. The $F_o - F_c$ electron density (red) in the right side of the panels is modeled at 3.0σ, and the $2F_o - F_c$ density (blue) in the left side view is modeled at 1.0σ. The conserved residues His56, Val97, Asp109, and Asn129 are shown for reference. Waters are depicted as red spheres. (a) Omit maps with neither azide nor dioxygen in the model of subunit A during refinement. (b) Maps from refinement with dioxygen covalently bound to the heme iron in the model of subunit A. (c) Maps from refinement with azide in the model of subunit A. (d) Maps of the same region of subunit B.

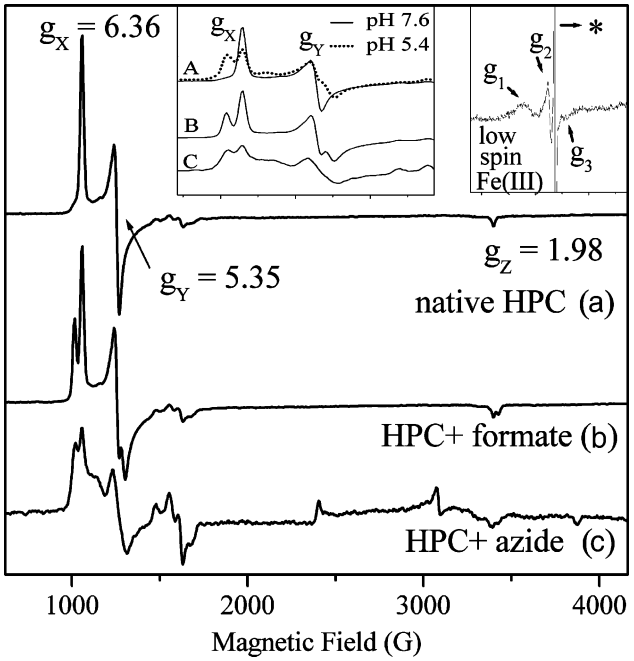

FIGURE 7: EPR spectra (9 GHz, 4 K) of the *H. pylori* catalase in the native state (a) and after treatment with formate (b) and azide (c), all at pH 7.6. Expansion of the low-field region ($g \approx 6$) of the spectra is shown in the center inset with the native enzyme spectrum at pH 5.4 (dotted line) superimposed on the pH 7.6 spectrum. Expansion of the low-spin ferric signal ($g_1 = 2.43$, $g_2 = 2.06$, and $g_3 = 1.87$) originating from a weak field ligand to the sixth position of the ferric heme iron is shown in the right inset. The narrow signal (denoted with an asterisk) corresponds to an organic radical.

Figure 9a. The results (Figure 9d) show that, indeed, the carboxylic proton is transferred to His56, while the second oxygen approaches the Fe^{3+} atom. The minimum energy conformation corresponds to a situation with the formate anion interacting not only with His56 H^+ and Asn129 but also with the heme iron 2.67 Å from the closest oxygen. This distance is very close to the Fe···O distance in subunit A (2.66 Å). Additional calculations in models not including any distal residues show that formate, but not formic acid, forms a strong bond with the heme iron.

DISCUSSION

The core structure of HPC is very similar in most respects to the structures of other catalases that have been reported. However, superimposed into this similar structure are a number of features that further our understanding of catalases. One of the first surprises arising from the structure is the lack of NADPH binding that is evident in the electron density maps and corroborated by a lack of binding to an affinity gel. This provides some corroboration to the earlier identification of residues His193, Arg202, Val301, and His304 (BLC numbering) as possible signatures for NADPH binding ability (*15*). In HPC, the equivalent four residues are Tyr175, Arg184, Ile283, and Thr286, and each of the three changes would interfere with NADPH binding through elimination of polar contacts or the introduction of direct steric conflicts. In addition, Trp179 replaces a Phe in BLC and would introduce another site of steric interference. The combination of these changes clearly precludes binding of NADPH to HPC at the site occupied in other catalases, and no substantial unassigned electron density was evident in the maps to suggest that it binds elsewhere. These results cannot preclude the possibility of weak binding of NADPH, either in a very different conformation or at some other site, that cannot be measured with an affinity column assay, but either possibility would make HPC different from other clade 3 enzymes.

Table 2: Characteristics of Bound Formic Acid

no.[a]	water displaced[b]	symmetry partner	protein contact
	(a) Heme Cavity and Channel		
1	+	2	y
2	+	1	y
3	+		y
4			
5	+		
6		7	
7	+	6	
8	+		y
	(b) Subunit Interface and Central Cavity		
13		35	y
15			
30	+		y
31	+	32	y
32	+	31	y
33	+	36	
35	+	13	y
36	+	33	
	(c) Dimer Interface		
10	++	20	y
11		21	
12	+	34	y
20	+	10	y
21	+	11	
34	+	12	y
	(d) Surface		
9	+	29	y
14	+		y
17	+		y
22	+		y
23		26	
24	+	28	y
25	+		
26		23	y
27	+		y
28		24	y
29	+	9	y
	(e) Random		
16	++		y
18	+		y
19	++		y

[a] The number in the coordinate file is this number plus 700. [b] +, one water displaced; ++, two waters displaced; y, contact with protein.

The main channel leading to the active site heme presents some subtle but surprising differences compared to other catalases. The first 15 Å from the heme to the conserved Asp109 is narrower than in all other catalases by 0.5−1.0 Å, and the partially roofed cavity structure of the upper channel above the conserved Asp differs considerably from the funnel shape in BLC, PMC, HEC, and CatF, from the partial cavity in CATA, and from the elongated narrow channel in MLC (Figure 5). Despite these differences, the kinetic parameters of turnover rate and H_2O_2 concentration at $^1/_2V_{max}$ for BLC (181 000 s^{-1} and 93 mM, respectively), MLC (284 000 s^{-1} and 147 mM, respectively), and HPC (250 000 s^{-1} and 108 mM, respectively) (*16*) are similar, indicating that small changes in the lower channel and substantial changes in the upper channel can be absorbed into the structure without a significant influence on catalysis.

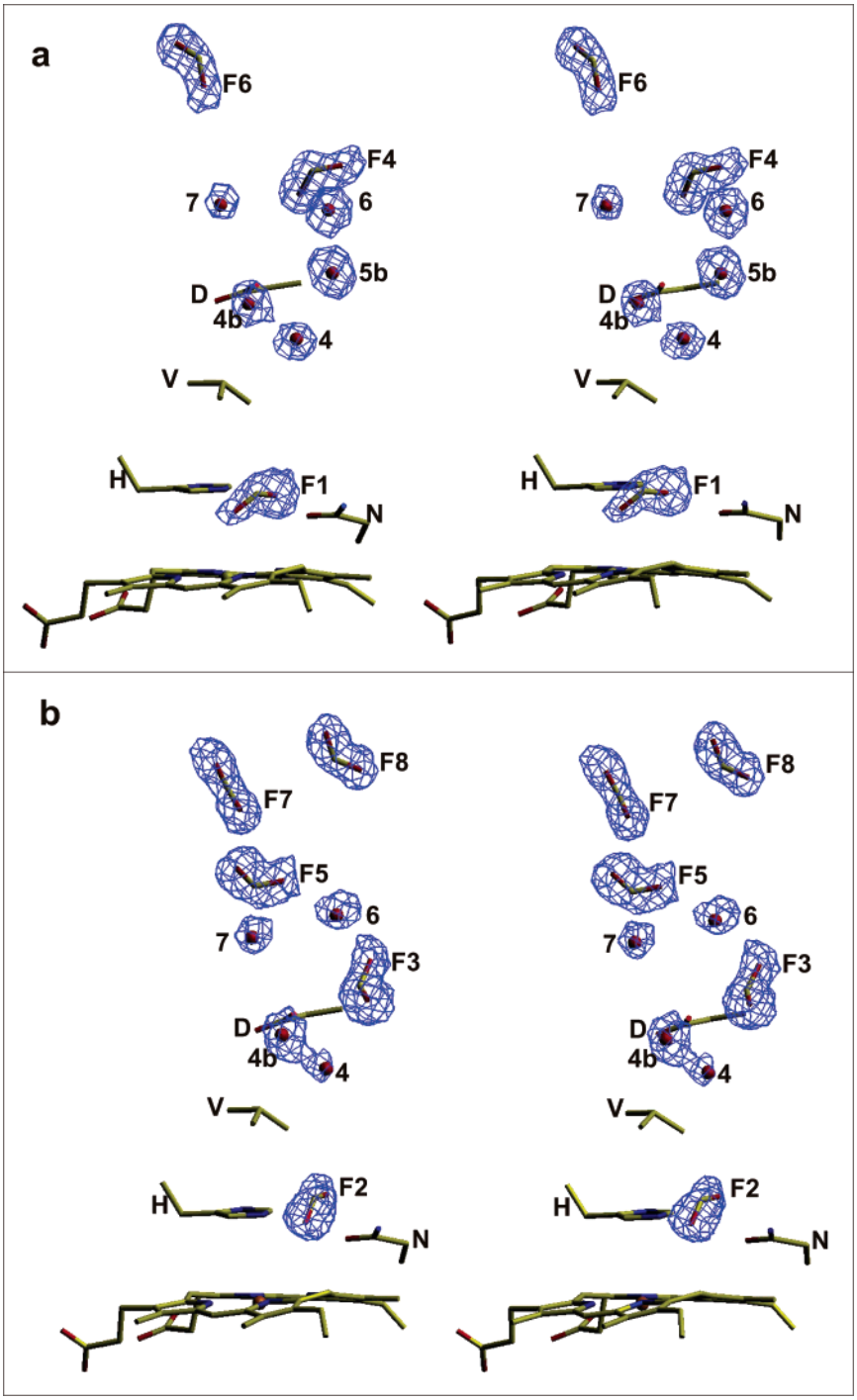

FIGURE 8: Stereoviews of the distal heme cavities of subunit A (a) and subunit B (b) showing the location of formic acids and waters. The $2F_o - F_c$ electron density (blue) is modeled at 1.0σ. The numbering of the formic acids is consistent with Table 2.

The elongated electron density associated with the iron in subunit B resembles the maps of oxymyoglobin (*44*) and compound III of horseradish peroxidase (*45*) more closely than the maps of compounds I and II of PMC (*46*) and MLC (*47*). If a peroxoferryl species is present, compound III with a perhydroxy or dixoygen group attached to the iron ($Fe^{III}-O-O-H$ or $H^+-Fe^{II}-O{=}O$) is more likely than either compound I or II which would not have survived the lengthy purification and crystallization processes. EPR studies confirm the presence of heme iron centers in the low-spin state, with *g* values consistent with water, a hydroxyl group, or a (hydro)peroxo substituent. Unlike previous cases of peroxo forms (*41*), no concomitant shift of the heme Soret band was detectable in the absorption spectrum of HPC. Conclusive identification will require further work. It is possible to explain the presence of a compound III-like species as being the result of the cells growing for 20 h with aeration combined with the lack of an NADPH-dependent mechanism for preventing compound II formation. Compound III would then arise from the interaction of compound II with an excess of H_2O_2.

The anticipated location for azide binding, based on CATA, is adjacent to the heme iron, and azide remains a possible solution to the electron density adjacent to the heme iron in subunit A. However, azide as a solution is not as satisfactory as a compound III-like solution, particularly

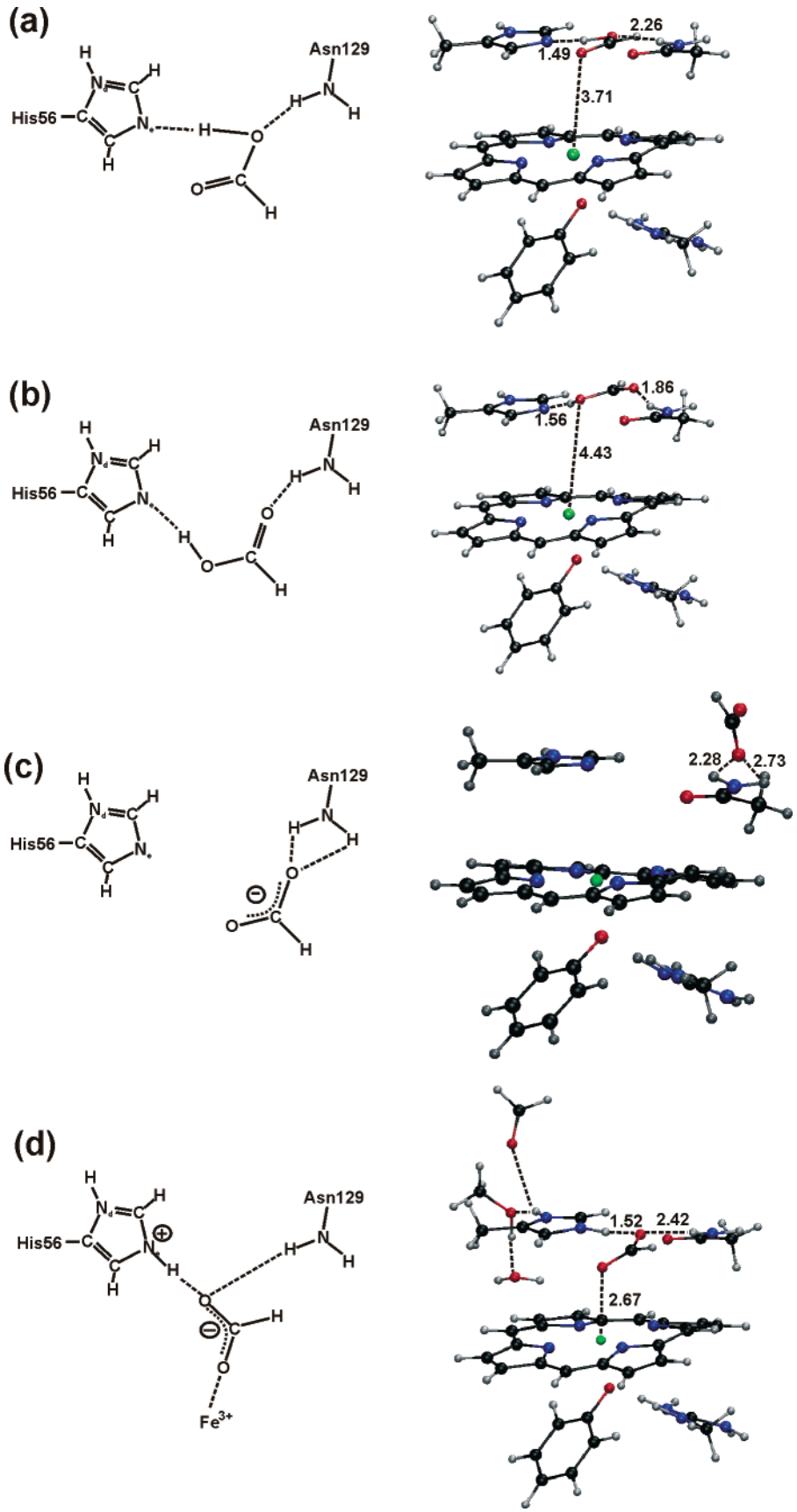

FIGURE 9: View of the two possible locations for formic acid (a and b), one possible location for formate ion alone (c), and one possible location for formate ion after protonation of the adjacent imidazole (d) determined by molecular dynamics calculations. On the right side of each panel are the optimized structures obtained from the calculations with the large model, starting with the ligand associated as shown on the left.

given the apparent covalent nature of the association between the ligand and the iron. Furthermore, EPR studies clearly show that azide is not directly coordinated to the heme iron. With an azide concentration of only 1.5 μM being sufficient

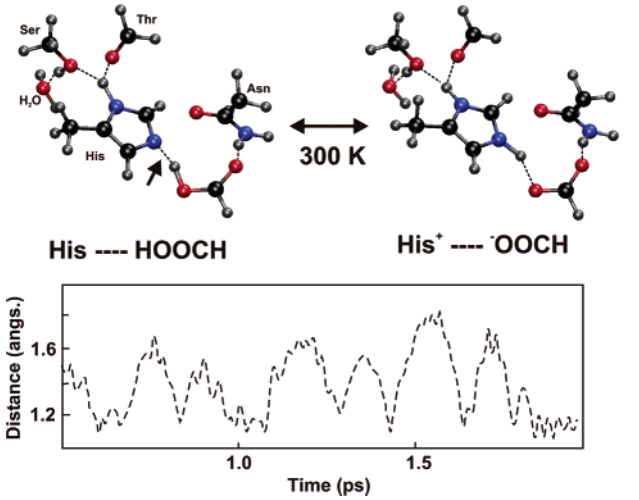

FIGURE 10: Fluctuation in the N$\epsilon\cdots$H distance during a portion of the Car−Parrinello simulation. The simulation was performed using the model with the ligand in the conformation shown in Figure 9b. The two extremes of hydrogen movement are shown in the top panel, and the fluctuation in bond length (indicated with an arrow) is shown in the bottom panel.

to cause 50% inhibition of HPC (*16*), 3 mM azide in the crystallization buffer should result in all azide binding sites being fully saturated, and yet no density is evident in the heme cavity of subunit B. Therefore, if the heme cavity is not the azide binding site, an alternative site lies on the *P* axis of the dimer where an azide-like species is bound. The spectral changes in the EPR ferric signal induced by azide treatment can be explained by geometry changes in the heme pocket induced from a distance. For example, the mutation of residues 10−12 Å from the heme affects the positioning of proximal residues, possibly including the heme axial ligand, causing changes in the EPR spectrum of a heme-containing catalase peroxidase (*48*). Accordingly, the azide molecule observed on the *P* axis of the dimer might induce repositioning of the axial ligand (Tyr339) via the links involving Arg47, Asp46, Tyr345, Tyr371, Asp341, and Ser338. Inhibition from a location ~15 Å from the heme presents an interesting mechanistic problem, however.

The asymmetric modification of only one subunit of the dimer of HPC to an apparent oxoferryl species provides support for the conjecture that only half of the catalase subunits are active (*49*). In the tetrameric structure of HPC, the compound III-modified subunits A and D are presumably inactive, while subunits B and C are active. There are parallels to this asymmetry in HEC where subunits A and D (revised designation from ref *15*) have NADPH bound and do not react with aminotriazole, suggestive of lower activity, whereas subunits B and C are active, as indicated by their reaction with aminotriazole. More questions than answers arise from these observations such as why NADPH is bound to the less active subunits of HEC, what differentiates subunits A and D (active) from subunits B and C (inactive), and what the functional reason or benefit in having half of the subunits inactive is. It is nonetheless fascinating that such asymmetry in reactivity is retained and evident in the crystal.

Spectroscopic work with BLC had concluded that one and possibly two formic acids were bound in the vicinity of the heme (*50*, *51*), and the results of the EPR experiments described above are consistent with this. In fact, the binding of 36 formates to HPC is not inconsistent with these conclusions because only one formate, that in subunit A which is 2.66 Å from the heme iron, would be close enough to the heme to cause a measurable spectral change. Degradation of compound II and of the putative compound III in subunit A may therefore be an alternate route for catalase regeneration to that of NADPH, which prevents compound II formation. Indeed, use of a simple metabolite for recovery of active enzyme from compounds II and III may be an example of a mechanism more primitive than that involving NADPH.

The protonation states of the His56 residue and formate ligand are difficult to determine experimentally, but the Car−Parrinello simulations reveal the following three points. First, a formate ion is unlikely to enter the heme distal pocket mainly because the combination of the formate anion and an unprotonated imidazole is unfavorable. Therefore, experimental electron density corresponding to the ligand in the heme cavity has to be interpreted mostly in terms of formic acid. Second, there are two similar hydrogen bonding configurations for the formic acid molecule with the ligand positioned 3.8 and 4.4 Å from the heme iron. This position agrees with the observed electron density in subunit B. Molecular dynamics simulations show that the proton from the formic acid is shared with the imidazole ring of His56, resulting in the imidazole being partially protonated and the formic acid partially unprotonated. Third, the combined interactions of the unprotonated formate ion with the Fe^{3+} cation, the Nϵ hydrogen of $His56^+$, and the NH_2 group of Asn129 offer an explanation for the shorter distance between the ligand and the heme iron in subunit A. In summary, the calculations in combination with experimental information indicate that it is formic acid that penetrates into the heme distal pocket, but that it will interact with the heme iron only after losing a proton to the essential histidine. The question that is not answered is why there is a difference between subunits A and B, but a difference in ability to polarize the formic acid OH group through the imidazole is suggested.

The structure of HPC does not provide any clues to explain the location of the catalase on the external surface of *H. pylori* cells. The N-terminal Met is visible in the structure, which might be taken as evidence that the catalase can be transported without processing a signal sequence. However, the enzyme used for this study was produced in *E. coli*, a foreign host, and catalases are not transported out of *E. coli*. The second question of how the enzyme might be retained on the *H. pylori* cell surface also is not answered by the structure. The N-terminus is not sufficiently extended to serve as a membrane anchor, and of the 16 disordered residues at the C-terminus, 12 are polar, including six Lys residues, three His residues, two Asp residues, and one Thr residue, making membrane attachment by this region unlikely.

NOTE ADDED IN PROOF

During the review of this paper, a paper describing the interaction of the catalase from *P. mirabilis* with formate appeared (*52*).

REFERENCES

1. Nicholls, P., Fita, I., and Loewen, P. C. (2001) Enzymology and structure of catalases, *Adv. Inorg. Chem. 51*, 51−106.

2. Murthy, M. R. N., Reid, T. J., Sicignano, A., Tanaka, N., and Rossmann, M. G. (1981) Structure of beef liver catalase, *J. Mol. Biol. 152*, 465−499.
3. Fita, I., Silva, A. M., Murthy, M. R. N., and Rossmann, M. G. (1986) The refined structure of beef liver catalase at 2.5 Å resolution, *Acta Crystallogr. B42*, 497−515.
4. Vainshtein, B. K., Melik-Adamyan, W. R., Barynin, V. V., Vagin, A. A., and Grebenko, A. I. (1981) Three-dimensional structure of the enzyme catalase, *Nature 293*, 411−412.
5. Vainshtein, B. K., Melik-Adamyan, W. R., Barynin, V. V., Vagin, A. A., Grebenko, A. I., Borisov, V. V., Bartels, K. S., Fita, I., and Rossmann, M. G. (1986) Three-dimensional structure of catalase from *Penicillium vitale*, at 2.0 Å resolution, *J. Mol. Biol. 188*, 49−61.
6. Murshudov, G. N., Melik-Adamyan, W. R., Grebenko, A. I., Barynin, V. V., Vagin, A. A., Vainshtein, B. K., Dauter, Z., and Wilson, K. (1982) Three-dimensional structure of catalase from *Micrococcus lysodeikticus* at 1.5 Å resolution, *FEBS Lett. 312*, 127−131.
7. Gouet, P., Jouve, H. M., and Dideberg, O. (1995) Crystal structure of *Proteus mirabilis* PR catalase with and without bound NADPH, *J. Mol. Biol. 249*, 933−954.
8. Bravo, J., Verdaguer, N., Tormo, J., Betzel, C., Switala, J., Loewen, P. C., and Fita, I. (1995) Crystal structure of catalase HPII from *Escherichia coli*, *Structure 3*, 491−502.
9. Bravo, J., Maté, M. J., Schneider, T., Switala, J., Wilson, K., Loewen, P. C., and Fita, I. (1999) Structure of catalase HPII from *Escherichia coli* at 1.9 Å resolution, *Proteins 34*, 155−166.
10. Berthet, S., Nykyri, L., Bravo, J., Maté, M. J., Berthet-Colominas, C., Alzari, P. M., Koller, F., and Fita, I. (1997) Crystallization and preliminary structural analysis of catalase-A from *Saccharomyces cerevisiae*, *Protein Sci. 6*, 481−483.
11. Maté, M. J., Zamocky, M., Nykyri, L. M., Herzog, C., Alzari, P. M., Betzel, C., Koller, F., and Fita, I. (1999) Structure of catalase-A from *Saccharomyces cerevisiae*, *J. Mol. Biol. 286*, 135−139.
12. Ko, T.-P., Safo, M. K., Musayev, F. N., Di Salvo, M. L., Wang, C., Wu, S.-H., and Abraham, D. J. (1999) Structure of human erythrocyte catalase, *Acta Crystallogr. D56*, 241−245.
13. Putnam, C. D., Arvai, A. S., Bourne, Y., and Tainer, J. A. (1999) Active and inhibited human catalase structures: ligand and NADPH binding and catalytic mechanism, *J. Mol. Biol. 296*, 295−309.
14. Carpena, A., Perez, R., Ochoa, W. F., Verdaguer, N., Klotz, M. G., Switala, J., Melik-Adamyan, W., Fita, I., and Loewen, P. C. (2001) Crystallization and preliminary X-ray analysis of clade I catalases from *Pseudomonas syringae* and *Listeria seeligeri*, *Acta Crystallogr. D57*, 1184−1186.
15. Carpena, X., Soriano, M., Klotz, M. G., Duckworth, H. W., Donald, L. J., Melik-Adamyan, W., Fita, I., and Loewen, P. C. (2003) Structure of the clade I catalase, CatF of *Pseudomonas syringae*, at 1.8 Å resolution, *Proteins 50*, 423−436.
16. Switala, J., and Loewen, P. C. (2002) Diversity of properties among catalases, *Arch Biochem. Biophys. 401*, 145−154.
17. Odenbreit, S., Wieland, B., and Haas, R. (1996) Cloning and genetic characterization of *Helicobacter pylori* catalase and construction of a catalase-deficient mutant strain, *J. Bacteriol. 178*, 6960−6967.
18. Nicholls, P., and Schonbaum, G. R. (1963) Catalases, in *The Enzymes* (Boyer, P., Lardy, H., and Myrback, K., Eds.) 2nd ed., Vol. VIII, pp 147−225, Academic Press, New York.
19. Collaborative Computational Project, Number 4 (1994) The CCP4 Suite: Programs for Protein Crystallography, *Acta Crystallogr. A50*, 760−763.
20. Evans, P. R. (1997) Scala, *Joint CCP4 and ESF-EACBM Newsletter 33*, 22−24.
21. Vagin, A., and Teplyakov, A. (1997) MOLREP: an automated program for molecular replacement, *J. Appl. Crystallogr. 30*, 1022−1025.
22. Murshudov, G. N., Vagin, A. A., and Dodson, E. J. (1997) Refinement of macromolecular structures by the maximum-likelihood method, *Acta Crystallogr. D53*, 240−255.
23. Jones, T. A., Zou, J. Y., Cowan, S. W., and Kjeldgaard, M. (1991) Improved methods for building protein models in electron density maps, *Acta Crystallogr. A47*, 110−119.
24. Kleywegt, G. J., and Jones, T. A. (1994) Detection, delineation, measurement and display of cavities in macromolecule structures, *Acta Crystallogr. D50*, 178−185.
25. Maté, M. J., Sevinc, M. S., Hu, B., Bujons, J., Bravo, J., Switala, J., Ens, W., Loewen, P. C., and Fita, I. (1999) Mutants that alter the covalent structure of catalase hydroperoxidase II from *Escherichia coli*, *J. Biol. Chem. 274*, 27717−27725.
26. Evans, S. (1993) SETOR: Hardware lighted three-dimensional solid model representations of macromolecules, *J. Mol. Graphics 11*, 134−138.
27. Hillar, A., Nicholls, P., Switala, J., and Loewen, P. C. (1994) NADPH binding and control of catalase compound II formation: comparison of bovine, yeast and *Escherichia coli* enzymes, *Biochem. J. 300*, 531−539.
28. Rovira, C., and Fita, I. (2003) The proximal hydrogen-bonded residue controls the stability of the compound II intermediate of peroxidases and catalases, *J. Phys. Chem. B 107*, 5300−5305.
29. Car, R., and Parrinello, M. (1985) Unified approach for molecular dynamics and density-functional theory, *Phys. Rev. Lett. 55*, 2471−2474.
30. Galli, G., and Parrinello, M. (1993) First-principle molecular dynamics, in *Computer Simulation in Chemical Physics* (Allen, M. P., and Tildsley, D. J., Eds.) NATO ASI Series C, Vol. 397, pp 261−313, Kluwer, Dordrecht, The Netherlands.
31. Carloni, P., Röthlisberger, U., and Parrinello, M. (2002) The role and perspective of ab initio molecular dynamics in the study of biological systems, *Acc. Chem. Res. 35*, 455−464.
32. Carloni, P., and Röthlisberger, U. (2001) Simulations of enzymatic systems: Perspectives from Car-Parrinello molecular dynamics simulations, in *Theoretical Biochemistry: Processes and Properties of Biological Systems* (Eriksson, L., Ed.) pp 215−251 Elsevier Science, Amsterdam.
33. Troullier, M., and Martins, J. L. (1991) Efficient pseudopotentials for plane-wave calculations, *Phys. Rev. B 43*, 1993−2006.
34. Louie, S. G., Froyen, S., and Cohen, M. L. (1982) Non-linear ionic pseudopotentials in spin-density-functional calculations, *Phys. Rev. B 26*, 1738−1742.
35. Becke, A. D. J. (1986) Density functional calculations of molecular bond energies, *Chem. Phys. 84*, 4524−4529.
36. Perdew, J. P. (1986) Density functional approximation for the correlation energy of the inhomogeneous electron gas, *Phys. Rev. B 33*, 8822−8824.
37. Ivancich, A., Jouve, H. M., Sartor, B., and Gaillard, J. (1997) EPR investigation of compound I in *Proteus mirabilis* and bovine liver catalases: formation of porphyrin and tyrosyl radical intermediates, *Biochemistry 36*, 9356−9364.
38. Patterson, W. R., Poulos, T., and Goodin, D. B. (1995) Identification of a porhyrin B cation radical in ascorbate peroxidase compound I, *Biochemistry 34*, 4342−4345.
39. Ivancich, A., Mazza, G., and Desbois, A. (2001) Comparative electron paramagnetic resonance study of radical intermediates in turnip peroxidase isozymes, *Biochemistry 40*, 6860−6866.
40. Davydov, R., Macdonald, I. D. G., Makris, T. M., Sligar, S. G., and Hoffman, B. M. (1999) EPR and ENDOR of catalytic intermediates in cryoreduced native and mutant oxy-cytochromes P450cam: mutation-induced changes in the proton delivery system, *J. Am. Chem. Soc. 121*, 10654−10655.
41. Ibrahim, M., Denisov, I. G., Makris, T. M., Kincaid, J. R., and Sligar, S. G. (2003) Resonance Raman spectroscopic studies of hydroperoxo-myoglobin at cryogenic temperatures, *J. Am. Chem. Soc. 125*, 13714−13718.
42. Peisach, J., Blumberg, W. E., Ogawa, S., Rachmilewitz, E. A., and Oltzik, R. (1971) The effect of protein conformation on the heme symmetry in high spin heme proteins as studied by electron paramagnetic resonance, *J. Biol. Chem. 246*, 3342−3355.
43. Bloom, H., Chance, B., and Litchfield, W. J. (1978) Effect of pH on bovine catalases as determined by electron paramagnetic resonance, *Biochim. Biophys. Acta 534*, 317−321.
44. Vojtechovsky, J., Chu, K., Berendzen, J., Sweet, R. M., and Schlichting, I. (1999) Crystal structures of myoglobin-ligand complexes at near atomic resolution, *Biophys. J. 77*, 2153−2174.
45. Berglund, G. I., Carlsson, G. H., Smith, A. T., Szöke, H., Henriksen, A., and Hajdu, J. (2002) The catalytic pathway of horseradish peroxidase at high resolution, *Nature 417*, 463−468.
46. Gouet, P., Jouve, H. M., Williams, P. A., Andersson, I., Andreoletti, P., Nussaume, L., and Hajdu, J. (1996) Ferryl intermediates of catalase captured by time-resolved Weissenberg crystallography and UV−Vis spectroscopy, *Nat. Struct. Biol. 3*, 951−956.
47. Murshudov, G. N., Grebenko, A. I., Brannigan, J. A., Antson, A. A., Barynin, V. V., Dodson, G. G., Dauter, Z., Wilson, K. S., and Melik-Adamyan, W. R. (2002) The structures of *Micrococcus*

lysodeikticus catalse, its ferryl intermediate (compound II) and NADPH complex, *Acta Crystallogr. D58*, 1972−1982.

48. Ivancich, A., Jakopitsch, C., Auer, M., Un, S., and Obinger, C. (2003) Protein-based radicals in the catalase-peroxidase of *Synechocystis* PCC6803: a multifrequency EPR investigation of wild-type and variants on the environment of the heme active site, *J. Am. Chem. Soc. 125*, 14093−14102.
49. Pelmont, J. (1989) Catalase, in *Enzymes*, pp 522−533, Grenoble Sciences, Grenoble, France.
50. Herschberg, R. D., and Chance, B. (1975) Optical and magnetic resonance studies of formate binding to horse liver catalase and sperm whale myoglobin, *Biochemistry 14*, 3885−3891.
51. Millar, F., Wrigglesworth, J. M., and Nicholls, P. (1981) Ligand binding to catalase and metmyoglobin, *Eur. J. Biochem. 117*, 13−17.
52. Andreoletti, P., Pernoud, A., Sainz, G., Gouet, P., and Jouve, H. M. (2003) Structural studies of *Proteus mirabilis* catalase in its ground state, oxidized state and in complex with formic acid, *Acta Crystallogr. D59*, 2163−2168.

BI035663I